Dependence of Crystallographic Orientation on Pitting Corrosion Behavior of Ni-Fe-Cr Alloy 028

LINA ZHANG, JERZY A. SZPUNAR, JIANXIN DONG, OLANREWAJU A. OJO, and XU WANG

The influence of crystallographic orientation on the pitting corrosion behavior of Ni-Fe-Cr alloy 028 was studied using a combination of X-ray diffraction (XRD), electron backscatter diffraction (EBSD), potentiodynamic polarization technique, and atomic force microscopy (AFM). The results show that there is anisotropy of pitting corrosion that strongly depends on crystallographic orientation of the surface plane. The distribution of pit density in a standard stereographic triangle indicates that the crystallographic planes close to {100} are more prone to pitting corrosion compared to planes {110} and {111}. The surface energy calculation of (001) and (111) shows that the plane with a high atomic packing density has a low surface energy with concomitant strong resistance to pitting corrosion. A correlation function between crystallographic orientation and pitting corrosion susceptibility suggests a method that not only predicts the pitting resistance of known textured materials, but also could help to improve corrosion resistance by controlling material texture.

I. INTRODUCTION

NICKEL-IRON-CHROMIUM (Ni-Fe-Cr) alloys are widely used in various industries and engineering sectors due to a combination of good mechanical properties and high corrosion resistance.[1–3] Ni-Fe-Cr alloy 028 (alloy 028) is a candidate particularly worth mentioning. The alloy 028 contains high amounts of nickel, copper, and molybdenum, which improve its resistance to corrosion attack in reducing mediums, and the high content of chromium makes the alloy more resistant to oxidizing species. Moreover, the alloy 028 is less expensive due to a higher amount of iron compared with other similar corrosion-resistant alloys. Currently, the alloy 028 is manufactured as evaporator tubes applied in phosphoric acid production; production tubing and casing used in deep and sour gas wells; heat exchangers employed in nuclear power plants, seawater-carrying piping; and seawater-cooled heat exchangers.[4–8] A number of investigations concerning corrosion performance in chloride ion mediums and under high-temperature environments containing different partial pressures of CO_2 and H_2S had been reported.[8–10]

Generally, alloy 028 tubulars are produced by a series of deformation processes, which are used to achieve certain requirements in mechanical properties and product dimensions. It is known that materials may form a preferred grain orientation (texture) during mechanical deformation processes. Previous research demonstrated that the crystallographic orientation can control dissolution, corrosion, and oxidation of materials.[11,12] However, there are few reports regarding the effect of crystallographic orientation on corrosion performance of the alloy. It is significant and imperative to investigate the influence of crystallographic orientation on corrosion resistance of the alloy 028.

The purpose of the present work is to evaluate the influence of crystallographic orientation on the pitting corrosion behavior of Ni-Fe-Cr alloy 028. X-ray diffraction (Bruker AXS diffraction system) and electro back scattering diffraction (EBSD) were applied to determine texture and crystallographic orientation distribution of the alloy 028. A potentiodynamic polarization technique was employed to examine pitting corrosion performance of the alloy in 0.5 M neutral sodium chloride solution. The morphology of the corroded surface was observed by using a scanning electron microscope (SEM) and atomic force microscopy (AFM). Based on statistical analysis, a correlation between crystallographic orientation and pitting corrosion behavior of the alloy 028 was developed.

LINA ZHANG and OLANREWAJU A. OJO are with the Department of Mechanical Engineering E2-327 EITC, University of Manitoba, Winnipeg, MB R3T 5V6, Canada. Contact e-mail: Lina.Zhang@umanitoba.ca JERZY A. SZPUNAR and XU WANG are with the Department of Mechanical Engineering, University of Saskatchewan, Saskatoon, SK S7N 5A9, Canada. JIANXIN DONG is with the School of Materials Science and Engineering, University of Science and Technology Beijing, Beijing 100083, China.

II. MATERIALS AND METHODS

The samples ($20 \times 20 \times 5$ mm^3) were cut from a commercial hot extruded pipe of alloy 028. Chemical composition of the tested material is listed in Table I. Prior to the experiment, samples were polished to obtain a mirror-like and strain-free surface. The polished specimens were cleaned in distilled water and were put in an acetone ultrasonic bath for 10 minutes, then dried at 30 °C.

The crystallographic texture was measured by Bruker AXS diffraction system with area detector and Cr $K\alpha$ radiation. The orientation distribution functions (ODFs) were calculated using TexTools programs. The detailed crystallographic orientation distribution (orientation imaging microscopy map) of a randomly chosen location was determined by using the SU 6600 Hitachi field emission scanning electron microscope (SEM) equipped with an Oxford Instruments NordlysNano EBSD detector. The AZTEC 2.0 data acquisition

Table I. Chemical Composition of Alloy 028 (Atomic Percent)

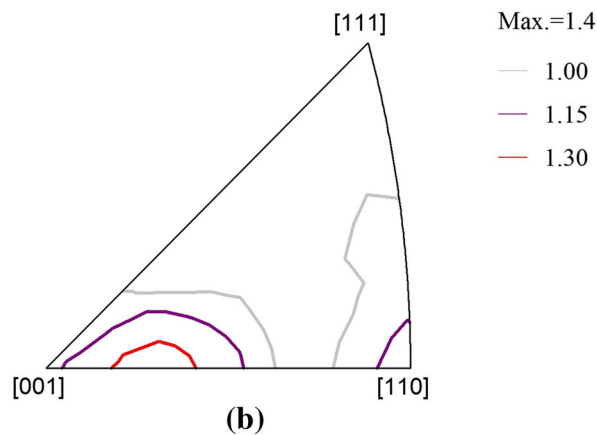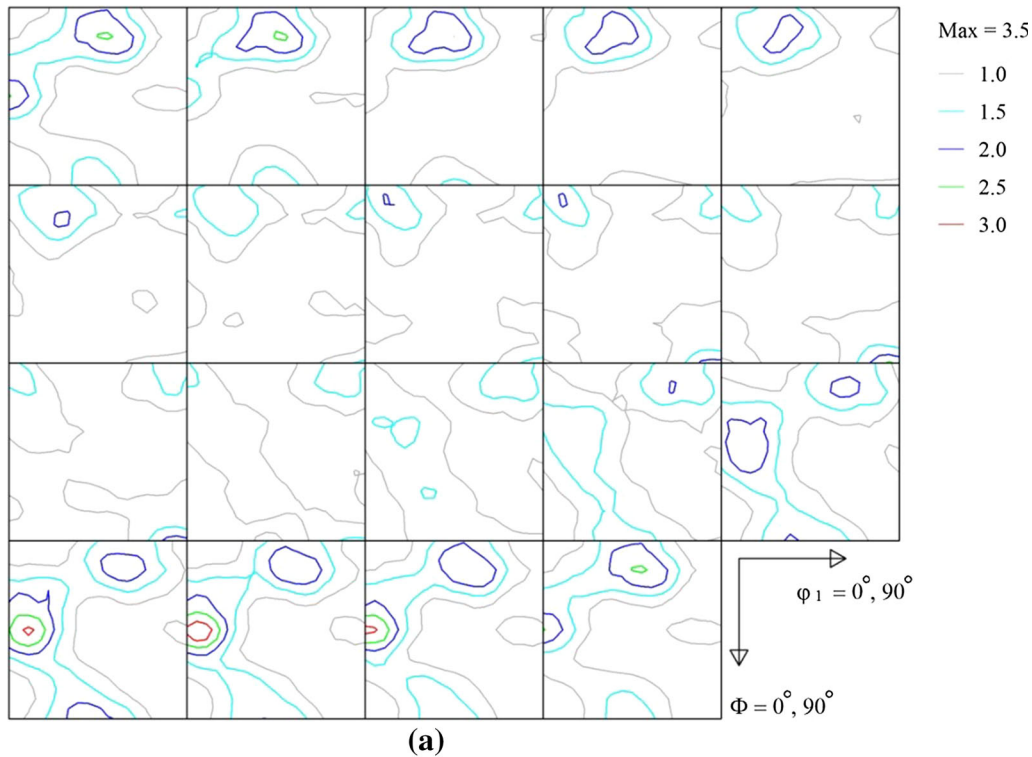| C	Si	Mn	Cr	Mo	Cu	Ni	Fe
0.066	0.34	0.72	28.38	2.27	0.88	30.01	bal.

Fig. 1—The crystallographic textures on the surface of alloy 028: (*a*) Orientation distribution function (ODF), (*b*) inverse pole figure (IPF) map, direction normal to the sample surface.

software was applied for indexing diffraction patterns to identify crystallographic orientations of the grains. Further analysis of EBSD data was carried out by employing the Oxford Instruments Channel 5 post processing software.

Electrochemical corrosion tests were performed under 0.5 M neutral sodium chloride (NaCl) solution. A graphite plate and standard calomel electrode (SCE) were used as counter and reference electrodes, respectively. Gamary Interface1000 Potentiostat system was employed for data acquisition. Prior to the electrochemical polarization experiment, an open circuit potential measurement was carried out for 60 minutes to achieve a stable corrosion potential. The polarization curves were obtained at a scan rate of 1 mV/s. All experiments were conducted at room temperature.

The SEM and atomic force microscopy (AFM) were employed to examine the corroded surface. The Nanoscope v6.13 Software was used to visualize 2D and 3D AFM images. The roughness profile of the surface was characterized by the mean roughness value R_a. Section analysis was used to measure the depth of pits. A correlation function between grain orientation and pitting corrosion sensibility was developed by employing the MatLab software.

III. RESULTS AND DISCUSSION

Figure 1 illustrates an orientation distribution function (ODF) and the normal direction inverse pole figure (IPF) of alloy 028, obtained by X-ray diffraction (XRD) measurement and TexTools calculation. It is demonstrated that the specimen exhibits a weak texture which indicates the distribution of crystallographic orientations is nearly random. The orientation imaging microscopy map (OIM) of the sample was examined by using EBSD, as shown in Figure 2, which determines the grain orientation distributions of a randomly selected area.

In order to investigate the influence of crystallographic orientation on pitting corrosion performance of the alloy 028, the specimen was polarized in 0.5 M neutral NaCl solution at room temperature. The potentiodynamic polarization test was carried out at a stabilized open circuit potential (OCP). Previous studies found that Cl^- ion, a relatively small ion, has a strong ability to adhere to the surface and to penetrate into the alloy substrate, thereby influencing the formation of passive films.[13,14] On the other hand, Cl^- ion may attach to some defects of the protective film and make contact with the metal matrix; in such cases, the rate of localized corrosion is accelerated which causes pitting or crevice corrosion.[15–18] Figure 3 depicts the polarization curve and the transpassivation occurring when the potential is above 1.05 V.

The corroded surface was examined by SEM, which exhibits nonuniform dissolution and corrosion. There are more pits which appear on some grains with certain orientations compared to other orientations. Figure 4 shows the randomly selected area of the specimen after polarization experiment provided as an example. Figure 4(a) illustrates the OIM map of this area, and the pit distribution on grains with different orientations is given in Figure 4(b). It is clear that the grains 2 and 3 that orientated close to {001} are more sensitive to pitting corrosion with round shape pits being observed on grains with this orientation. Several pits appear on grain 1 with a crystallographic orientation close to {101}, while grains 5 and 6 with an orientation close to {111} have the best
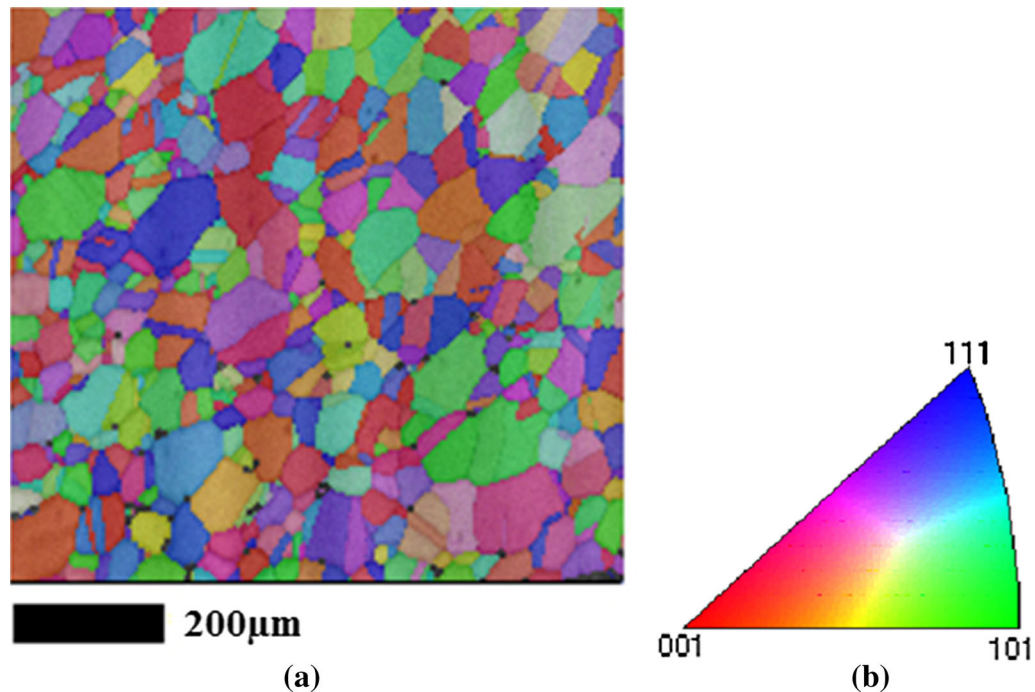

(a)   **(b)**

Fig. 2—EBSD orientation map: (*a*) Orientation imaging microscopy map (OIM) at a random location, (*b*) Legend for OIM.

corrosion resistance with no pits present on these grains. Hence, the results suggest that the pitting corrosion behavior of the alloy 028 is significantly dependent on the crystallographic orientation.

For better understanding the pitting behavior of the specimen, AFM was applied to observe morphology of the corroded area. Figure 5 depicts the 3D surface topography of grains suffering pitting corrosion. Grain 1 is close to {101}, grain 2 is close to {001}, and grain 5 is near to {111}. The surface roughness value increases in the order of grain, 5 < 1 < 2. The depth of the pits (dark spots) gathered in grain 2 is shown in Figures 5(c) through (f). As the results demonstrate, the corroded surface roughness depends on the crystallographic orientation as well.

To investigate the influence of crystallographic orientation on pitting corrosion performance of the alloy 028,

Fig. 3—Potentiodynamic polarization curve of alloy 028 in 0.5 M neutral NaCl solution at room temperature.

statistical analysis of pit number was done on the area with identified crystallographic orientation (whole EBSD scan area $750 \times 750\ \mu m$). The pit density (D_{pi}) of any orientation i was calculated as follows:

$$D_{pi} = \frac{N_p}{N_g}, \qquad [1]$$

where N_p is the pit number of grains with certain orientation i, and N_g is the grain number of that orientation i.

A figure illustrating the pit frequency in a standard stereographic orientation triangle is given in Figure 6. Figure 6(a) shows the normal direction IPF of this area, which exhibits a random distribution of crystallographic orientation. The distribution pit density is depicted in Figure 6(b). The quantitative results indicate that an anisotropic pit distribution significantly depends on crystallographic orientation. Noticeably, the highest frequency of pits occurs on grains with an orientation close to {001}, which suggests this crystallographic plane is very sensitive to pitting corrosion attack. A few pits are present on planes near to {101} and {111}.

The pitting corrosion, as a local form of corrosion, strongly relates with the local surface reactivity.[19] The most fundamental electronic properties of a metallic surface can be characterized by the surface free energy and work function, which are beneficial to understand a wide range of surface phenomena of alloys.[20] Pitkänen and his co-workers provided a method to calculate the surface energy of $Fe_{1-c-n}Cr_cNi_n$ random alloys using the Ab initio calculation.[21] The surface energy of two low index planes of {001} and {111} are calculated by the following Eqs. [2] and [3]:

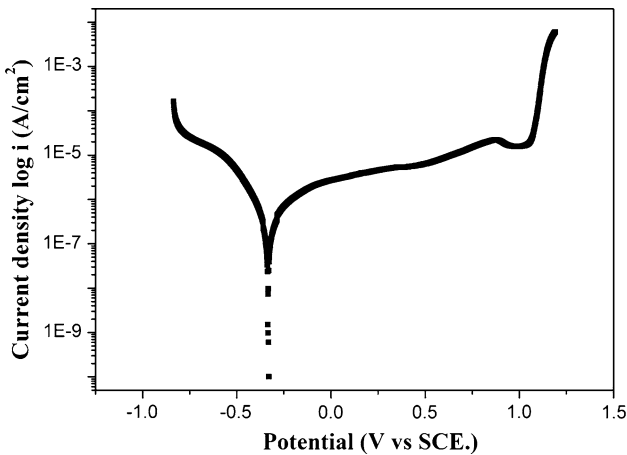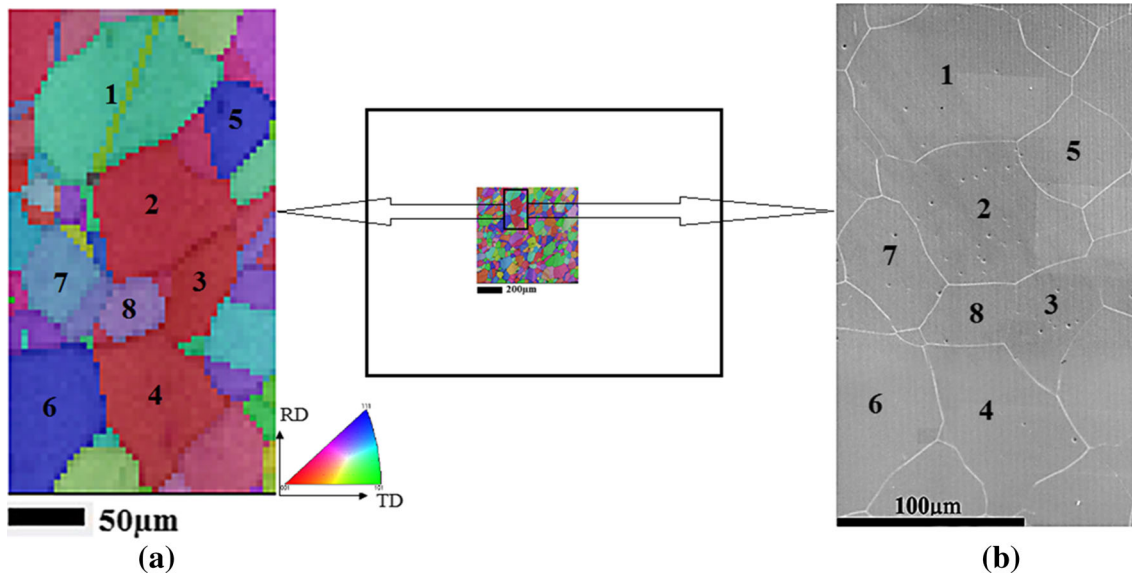$$\gamma(001) = 1.042c - 0.228n + 2.926 \quad [J/m^2] \qquad [2]$$

Fig. 4—A randomly selected area on the surface of alloy 028: (*a*) OIM map, (*b*) SEM image for the same area after pitting corrosion in 0.5 M neutral NaCl solution at room temperature.
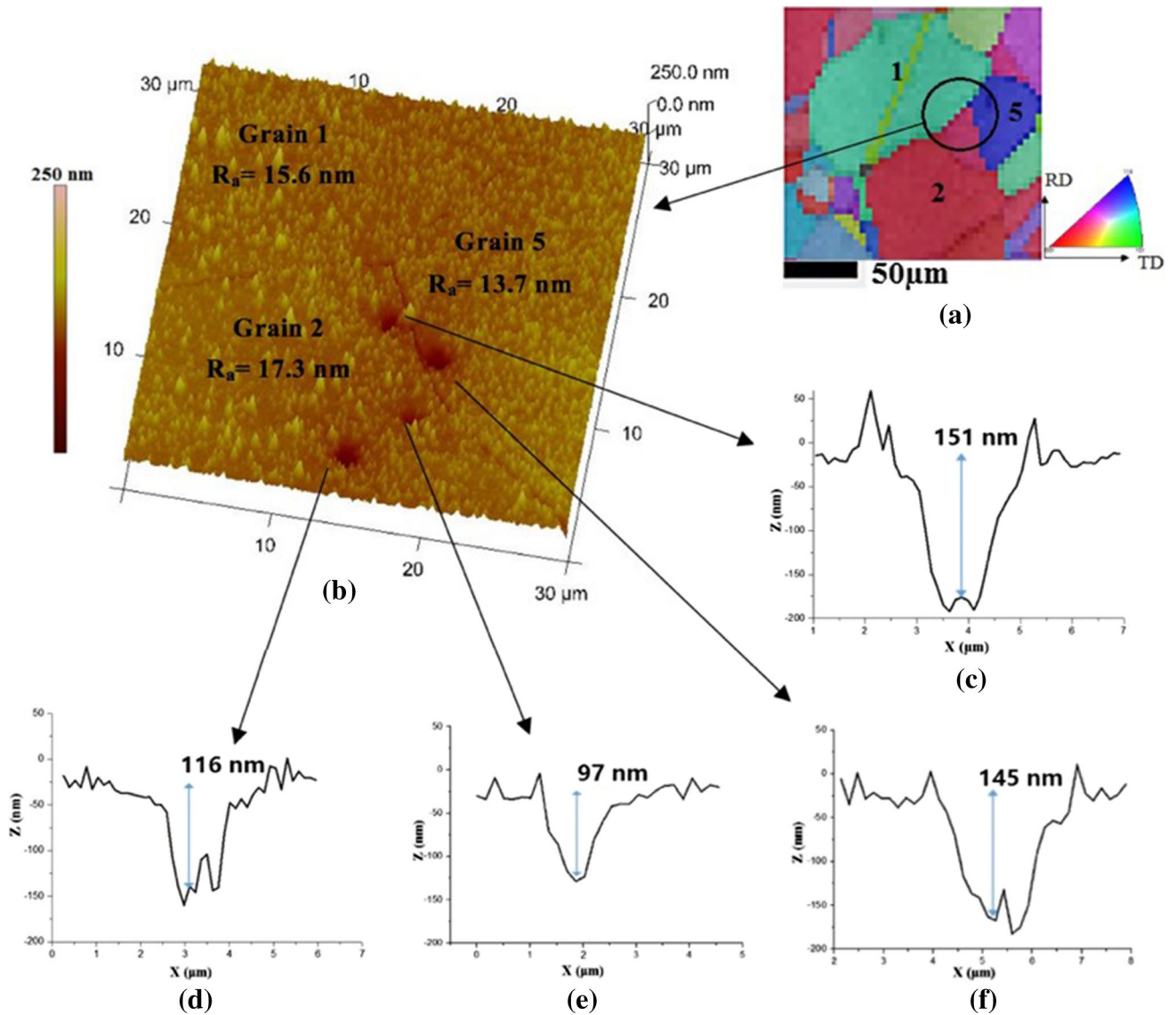
Fig. 5—AFM topography of grains of alloy 028 after pitting corrosion in 0.5 M neutral NaCl solution at room temperature: (*a*) OIM map, (*b*) 3D surface topography, (*c*) through (*f*) section analysis of pit depth.

$$\gamma(111) = 1.279c - 0.143n + 2.588 \quad [\text{J/m}^2], \qquad [3]$$

where the element concentration range is $0.12 \leq c \leq 0.32$ and $0.04 \leq n \leq 0.32$ (in atomic fraction).

Therefore, based on the aforementioned formulae, we calculate the surface energy of these specific planes for alloy 028 ($c = 0.2838$ and $n = 0.3001$). The results show that $\gamma(001) = 3.1533$ J/m^2 and $\gamma(111) = 2.9081$ J/m^2. Compared to the crystal plane (001), the crystal plane (111) has a lower surface energy and better resistance to pitting corrosion. The surface energy shows an inverse relationship with the density of atomic packing,[12] which means that atoms on the low surface energy planes have a high density in atomic packing. It is well known that for face-centered cubic (FCC) structural systems, the {111} and {101} planes are more closely packed, and the atoms on these planes have larger binding energies, compared to less closely packed plane, such as {001}.[22,23] Thus, the closely packed planes are more resistant to dissolution, and the activation energy of dissolution is increased with the increase in atomic packing density. Gaillard and his colleagues reported a relationship between the crystallographic orientation and work function of FCC polycrystalline materials.[24] The results illustrate that each crystallographic orientation has a specific surface potential; more specifically, the denser face {111} has a higher work function value, followed by the {110} and {100} which have medium and low work function values, respectively.[24] It has been demonstrated that for polycrystalline Mg, the basal plane (high-density packing plane {0001}) with low surface energy presents a more positive corrosion potential, which means it is more resistant to corrosion than other planes.[25]
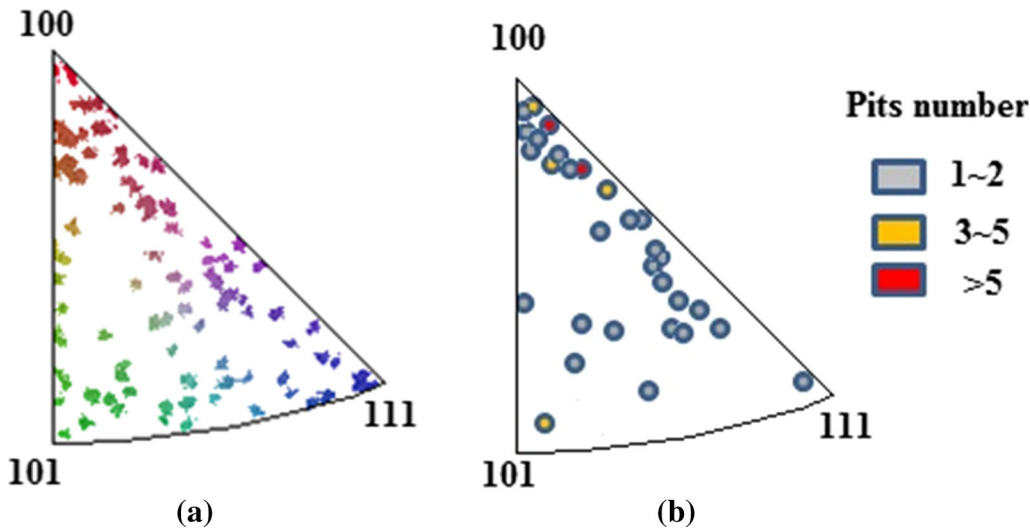
Fig. 6—Standard stereographic triangle with various crystallographic planes: (*a*) distribution of grain orientation, (*b*) distribution of pits density.

Table II. The Values of the Constants

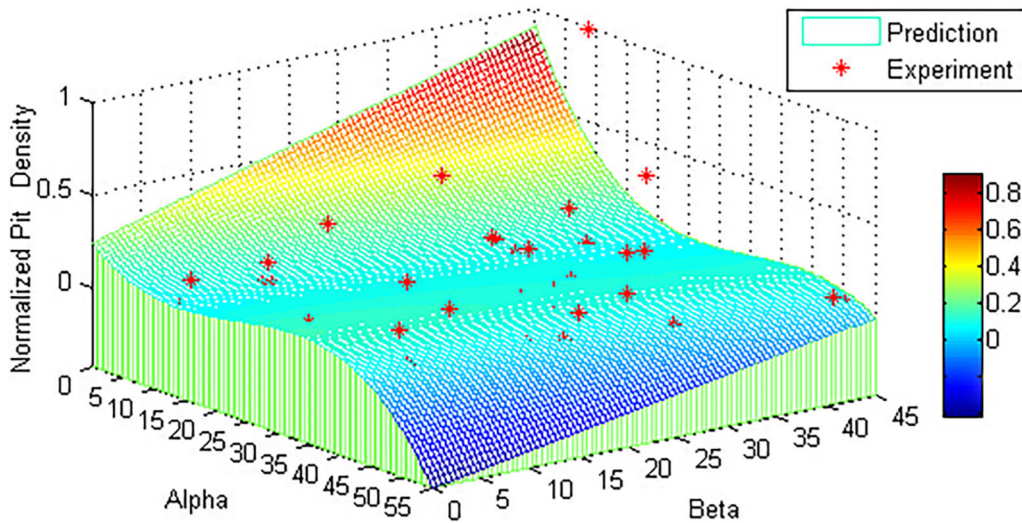| Constant	K_0	K_1	K_2	K_3	K_4	K_5	K_6
Value	0.2436	0.0309	0.0016	2.285×10^{-5}	0.0146	0.00108	1.77×10^{-5}

Fig. 7—Graphical representation of distribution of pitting corrosion susceptibility (the coordinates are the spherical polar coordinates, 0 deg $\leq \alpha \leq$ 53 deg, 0 deg $\leq \beta \leq$ 45 deg).

Since the pitting corrosion behavior depends on crystallographic orientation, establishing a correlation between the crystallographic orientation and pitting corrosion susceptibility is beneficial in predicting pitting corrosion performance. For this purpose, the pit density of different oriented grains is normalized using the following Eq. [4]

$$D_{\mathrm{n}} = \frac{D_{pi}}{D_{\mathrm{pmax}}}, \qquad [4]$$

where D_{pi} represents the pit density of any orientation i, D_{pmax} is the maximum pit density, and the range of D_n is $0 \leq D_n \leq 1$.

The normalized pit density of any specific crystallographic orientation can be used to evaluate the pitting corrosion susceptibility for this specific orientation. For the FCC structural systems, the spherical polar coordinates (0 deg $\leq \alpha \leq$ 53 deg, 0 deg $\leq \beta$ deg $\leq$ 45 deg) can be used to describe the orientation of crystallographic plane (hkl). The normalized pit density D_{n} obtained
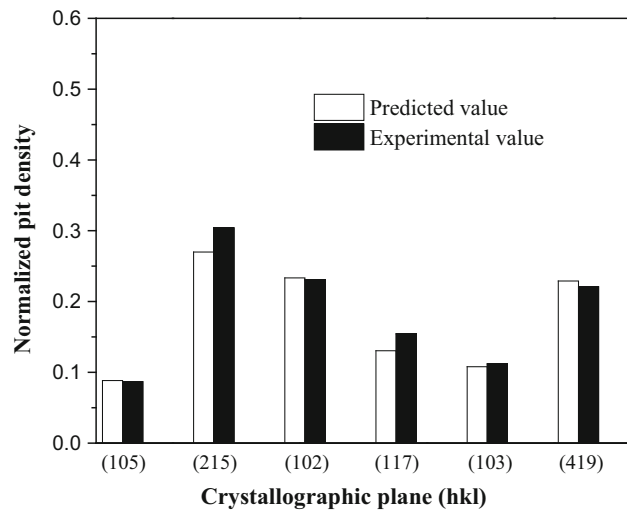
Fig. 8—The deviation between the predicted pitting corrosion susceptibility and experimental data for randomly selected crystallographic planes.

from experimental orientation-pitting data is described as a function of the spherical polar coordinates (α, β) given by the following Eqs. [5] through [7]

$$D_n(\alpha, \beta) = K_0 + \alpha f_1(\alpha) + \beta f_2(\alpha) \qquad [5]$$

with

$$f_1(\alpha) = K_1 + K_2\alpha + K_3\alpha^2 \qquad [6]$$

$$f_2(\alpha) = K_4 + K_5\alpha + K_6\alpha^2 \qquad [7]$$

The constant values $K1$ to $K6$ are listed in Table II. A novel model is developed to predict pitting corrosion susceptibility of different crystallographic orientation by using the MatLab software. Figure 7 illustrates a comparison between the predicted results obtain from the developed model and experimental results. The deviation between the predicted value of pitting corrosion susceptibility and experimental data for randomly selected crystallographic planes is given in Figure 8, which suggests the predicted values generally agree with the experimental data. Therefore, this method could be used not only to evaluate pitting corrosion resistance of a certain crystallographic orientation plane, also to predict the pitting corrosion susceptibility of the given textured material.

IV. CONCLUSIONS

The influence of crystallographic orientation on pitting corrosion performance of Ni-Fe-Cr alloy 028 was studied by the XRD, EBSD, AFM and potentiodynamic polarization techniques. The results suggest that the most sensitive surface to pitting corrosion are planes oriented close to {001}, while planes {111} and {101} with high atomic density have higher pitting corrosion resistance. The pit frequency distribution triangle based on the IPF characterizes the dependence of pitting corrosion behavior of an alloy on crystallographic orientation. A novel model is developed to predict the susceptibility of pitting corrosion performance for a given textured alloy.

REFERENCES

1. E.L. Hibner, C.S. Tassen: Corrosion, 2001, Paper No. 01102, NACE International, Houston, TX, USA, 2001.
2. A. Thomas, M. EI-Wahabi, J.M. Cabrera, and J.M. Prado: J. Mater. Process. Technol., 2006, vol. 177, pp. 469–72.
3. S. Ghosh and T. Ramgopal: Corrosion, 2005, vol. 61, pp. 609–19.
4. D. Bankiewicz, P. Vainikka, D. Lindberg, A. Frantsi, J. Silvennoinen, P. Yrjas, and M. Hupa: Fuel, 2012, vol. 94, pp. 240–50.
5. U. Kivisäkk: Corros. Sci., 2003, vol. 45, pp. 485–95.
6. X. Gómez and J. Echeberria: Mater. Sci. Eng., A, 2003, vol. 348, pp. 180–91.
7. N. Xian, M. Rong, F. Jiang, L.H. Li, and D.Y. Shi: Corrosion, 2012, vol. 68, pp. 620–24.
8. T. Bellezze, G. Roventi, and R. Fratesi: Electrochim. Acta, 2004, vol. 49, pp. 3005–14.
9. C.F. Chen, R.J. Jiang, G.A. Zhang, S.Q. Zheng, and L. Ge: Rare Metal Mater Eng, 2010, vol. 39, pp. 427–32.
10. A.L. Wei, G.X. Zhao, K. Liu, and W.T. Cai: J. Xi'an Shiyou Univ., 2011, vol. 26, pp. 68–75.
11. W. Wang and A. Alfantazi: Electrochim Acta, 2014, vol. 131, pp. 79–88.
12. R. Bès, S. Gvarini, N. Millard-Pinard, S. Cardinal, A. Perrat-Mabilon, C. Peaucelle, and T. Douillard: J. Nucl. Mater., 2012, vol. 427, pp. 415–17.
13. M.V. Cardoso, S.T. Amaral, and E.M.A. Martini: Corros. Sci., 2008, vol. 50, pp. 2429–36.
14. X.M. Bi and C.N. Cao: J. Chin. Soc. Corro. Prot., 1983, vol. 3, pp. 199–216.
15. H. Altun and S. Sen: Mater. Des., 2004, vol. 25, pp. 637–43.
16. L.N. Zhang, J.A. Szpunar, J.X. Dong, and M.C. Zhang: J. Mater. Res., 2014, vol. 29, pp. 2147–55.
17. A. Dhanapal, S. Rajendra Boopathy, and V. Balasubramanian: J. Alloys Compd., 2012, vol. 523, pp. 49–60.
18. A. Bouzoubaa, B. Diawara, V. Maurice, C. Minot, and P. Marcus: Corros. Sci., 2009, vol. 51, pp. 2174–82.
19. V. Vignal, H. Krawiec, O. Heintz, and R. Oltra: Electrochim. Acta, 2007, vol. 52, pp. 4994–5001.
20. H.L. Skriver and N.M. Rosengaard: Phys. Rev. B, 1992, vol. 46, pp. 7157–68.
21. H. Pitkänen, M. Alatalo, A. Puisto, M. Ropo, K. Kokko, and L. Vitos: Surf. Sci., 2013, vol. 609, pp. 190–94.
22. H. Park and J.A. Szpunar: Corro. Sci., 1998, vol. 40, pp. 525–45.
23. J.M. Zhang, F. Ma, and K.M. Xu: Appl. Surf. Sci., 2004, vol. 229, pp. 34–42.
24. N. Gaillard, D. Mariolle, F. Bertin, M. Gros-Jean, M. Proust, A. Bsiesy, A. Bajolet, S. Chhun, and M. Djebbouri: Microelectr. Eng., 2006, vol. 83, pp. 2169–74.
25. G.L. Song and Z.Q. Xu: Corro. Sci., 2012, vol. 63, pp. 100–12.